JAAS

ROYAL SOCIETY OF CHEMISTRY

PAPER

View Article Online
View Journal | View Issue

Cite this: *J. Anal. At. Spectrom.*, 2026, **41**, 1869

Interlaboratory comparison of XRF analysis on thin films, including alloys, oxides, multilayers, and a lithium-ion battery material

André Wählisch, *[a] Cornelia Streeck, [a] Yannick Philipp Stenzel, [b] Sascha Nowak, [b] Markus Osenberg, [c] Ingo Manke, [c] Michael Fartmann, [d] Birgit Hagenhoff, [d] Rainer Unterumsberger, [e] Malte Wansleben, [e] Lars Anklamm, [e] Markus Krämer, [f] Peter Gawlitza, [g] Elena Blokhina [h] and Burkhard Beckhoff [a]

We report on a comprehensive, international interlaboratory comparison of multiple thin film samples, including pure metals, stoichiometric oxides, multilayers consisting of three different metals, non-stoichiometric alloys, and a lithium-ion battery material based on nickel, manganese, and cobalt oxides. The thickness of the layers ranged from a few tens of nanometers to about one micrometer, depending on the type of thin film. The participants of the interlaboratory comparison analyzed the samples using X-ray fluorescence analysis and a relative standard deviation of the results ranging from about 3% to 17% was observed, with thicker alloy samples tending to perform worse. An extensive pre-characterization scheme was used in the form of different complementary analytical techniques such as X-ray reflectometry, time-of-flight secondary ion mass spectrometry, and X-ray tomography. Synchrotron-based reference-free X-ray fluorescence analysis measurements were used to determine physically traceable results. Using such a variety of independent methods ensured a robust overall validation approach. This corroborates that calibration samples for such thin films can be designed, produced, and qualified in a flexible and straightforward manner. These calibration samples can easily be integrated into process control for a variety of application fields, including X-ray fluorescence analysis and other techniques.

Received 19th November 2025
Accepted 10th April 2026

DOI: 10.1039/d5ja00460h

rsc.li/jaas

Introduction

X-ray fluorescence (XRF) analysis can be used to both identify and quantify the chemical elements contained in a material, and is widely employed in a very broad range of industrial and scientific applications[1] due to its suitability for rapid, nondestructive and automated analysis. XRF analysis often requires minimal, or no sample preparation and general-purpose instruments can be applied to an extremely wide range of chemical elements in various physical configurations. The principles of XRF are well-known[2–4] and, with appropriate analytical effort, reliable results with uncertainties in the low percentage range can be obtained. To ensure accurate interpretation of measured intensities, however, several nonlinear effects, such as instrumental response and sample-dependent effects, need to be considered, either directly or by an appropriate pre-calibration. Importantly, X-ray absorption and secondary X-ray fluorescence effects must be taken into account for samples containing multiple chemical elements and thicknesses greater than a few hundred nanometers, such as many application-critical thin films and bulk samples.[5–7] A classic example where secondary X-ray fluorescence can lead to significant contributions are steels,[8] where the excitation of one main constituent (*e.g.* iron) in the alloy may induce significant amounts of X-ray fluorescence radiation of another chemical element (*e.g.* chromium). Moreover, in other technological developments, such as solar cells[9] (*e.g.* copper indium gallium selenide) and battery materials[10] (*e.g.* lithium nickel manganese cobalt oxides), the use of increasingly complex layers in terms of composition is becoming more important. In such systems, secondary effects lead to stronger nonlinear correlations between elemental content and measured fluorescence intensity. However, the availability of suitable certified reference

[a]*Physikalisch-Technische Bundesanstalt (PTB), Abbestr. 2-12, 10587 Berlin, Germany. E-mail: andre.waehlisch@ptb.de*
[b]*MEET-Münster Electrochemical Energy Technology, Corrensstr. 46, 48149 Münster, Germany*
[c]*Helmholtz-Zentrum Berlin, Hahn-Meitner-Platz 1, 14109 Berlin, Germany*
[d]*Tascon GmbH, Mendelstr. 17, 48149 Münster, Germany*
[e]*Helmut Fischer GmbH, Rudower Chaussee 29-31, 12489 Berlin, Germany*
[f]*AXO DRESDEN GmbH, Gasanstaltstr. 8B, 01237 Dresden, Germany*
[g]*Fraunhofer-Institut für Werkstoff- and Strahltechnik IWS, Winterbergstr. 28, 01277 Dresden, Germany*
[h]*Bruker Nano GmbH, Am Studio 2D, 12490 Berlin, Germany*

materials (CRM) or qualified calibration samples often required for reliable analysis of such increasingly complex material systems is inherently extremely limited due to the high cost of designing, producing and characterizing them.[11] Especially in the commercial sector, there are only very few suppliers offering a limited number of SI-traceable thin film standards,[12] and these are almost exclusively for single-element films.

In general, interlaboratory comparisons (also known as round-robin tests or proficiency testing[13,14]) can help to evaluate analytical procedures,[15,16] specifically to verify reproducibility and repeatability of a technique,[17] or simply to identify problematic instruments. The present work addresses thin films in the thickness range from a few tens of nanometer to about one micrometer and presents the design principle, their fabrication and complementary characterizations of samples that can be readily qualified as calibration samples using the described methodology. Building on similar work,[18] this includes thin films of a single pure metal and stoichiometric oxides, multilayers, non-stoichiometric alloys and a lithium-ion battery material. As part of the present work, 17 different samples from these sample categories were prepared and used in an international XRF interlaboratory comparison to establish the viability of the methodology. Results of the comparison are validated by underpinning them with additional independent measurements: X-ray reflectivity was used to control film thickness and density of the thin films at the production stage. Individual time-of-flight secondary ion mass spectrometry measurements were performed to investigate ageing of the materials. Tomographic measurements were conducted to confirm the spatial homogeneity of the lithium-ion battery material. Furthermore, gravimetric methods were applied, to demonstrate the feasibility of measuring total mass (in μg) and total area (in cm^2) in comparison with XRF results that provide mass deposition per unit area (*e.g.* in μg cm^{-2}), even for thin films deposited on a wafer. Moreover, the reference-free approach of XRF by PTB[11,19] was used to ensure traceability of the XRF results. Ultimately, this work demonstrates that materials such as those used in the presented interlaboratory comparison can be produced in a flexible and scalable manner, and subsequently qualified as calibration specimens or reference materials.

Experimental

Design, production, and preparation of samples

Sample design. For the interlaboratory comparison, 17 different samples – including single layers, oxides, multilayers, alloys – were selected to cover a wide range of sample parameters, including composition, thickness, and matrix effects. This diversity allowed a robust comparison assessing analytical performance across several conditions, which are representative of typical applications. The samples are listed in Table 1 and can be divided into five different sample type categories: type 1 were five single layers of pure metals with thicknesses below 200 nm; type 2 were three different oxide layers with thicknesses below 150 nm; type 3 were four different multilayer systems containing three separate layers, each consisting of a pure metal; type 4 were four non-stoichiometric alloys consisting of three different metals; type 5 was a lithium-ion battery (LIB) electrode material, NMC622. All participants received a nominally identical copy of each sample at the same time, and for each individual sample, all specimen distributed to participants were from the same production batch to ensure comparability. For the oxide samples of type 2, the stoichiometric composition of the stable oxide was assumed, which is reasonable given the deposition process. This is because most participants' XRF instruments cannot detect oxygen itself.

The samples were designed to include simple monolayers (type 1), which should be straightforward to analyze using XRF; samples requiring a more sophisticated approach to analysis, by including stoichiometric oxides (type 2); and samples of increased compositional complexity (types 3 to 5), where the different chemical elements were selected to induce the secondary fluorescence effect: all samples of type 3 to 5 (multilayers, alloys, and LIB material) contain at least three chemical elements, two of which can have their XRF signal enhanced by the third. A design objective of the samples was that the secondary fluorescence process, where the XRF radiation of one element can enhance the X-ray fluorescence radiation of another chemical element, should contribute in the order of at least 10% to the XRF signal intensity for at least one element. This effect is strongest in the LIB material, potentially contributing up to 20% or more, depending on the exact excitation conditions. Tertiary fluorescence overall contributes less than 1% and, consequently, can be neglected in the present study.

Single layer, multilayer and alloy samples (type 1–4). Single layers, oxides, multilayers, and alloy samples (type 1–4) were produced using vacuum sputter deposition, namely magnetron sputter deposition and ion beam sputter deposition (see for example[20]). For these techniques, noble gas ions are activated in a plasma and accelerated towards a sputter target, typically a pure element such as metals or non-metals (*e.g.* silicon or carbon). Subsequently, atoms are released from the sputter target and deposited onto the actual substrate located at a predefined position in the coating chamber. This enables the targeted production of very stable, ultra-pure, very smooth and laterally extremely homogeneous thin layers or layer stacks, *i.e.* layers of typically one, a few or a few tens of nm with pm-level precision. Lateral thickness variations of less than 0.2% can be routinely achieved over distances of several tens of centimeters, and microroughness values are typically in the sub-nanometer range.[21,22] In practice, the choice of materials is limited only by the availability of suitable target materials. By adding reactive components to the process gas (*e.g.* oxygen), chemical compounds (*e.g.* oxides) can be produced when sputtering pure element targets. Some compounds, such as B_4C, can also be used directly as target material.

To create alloys with non-stoichiometric compositions (samples of type 4), several tens up to hundreds of thin nanolayers were deposited, alternating the pure constituents. For example, for a TiMnNi alloy, a sequence of Ti on Mn on Ni is deposited several times, with each chemical element deposited at a predefined and possibly different thickness to achieve the

Table 1 Overview of the 17 thin layer samples used in the interlaboratory comparison

#	Sample category	Layer sequence (top to bottom, on Si wafer substrate)	Target deposition thicknesses	Notes
1	Type 1 (single layer)	**Sc**	13.2 nm	
2	Type 1 (single layer)	**Sc**	56.6 nm	
3	Type 1 (single layer)	**Sc**	100 nm	
4	Type 1 (single layer)	**Ti**	185 nm	
5	Type 1 (single layer)	**Co**	70 nm	The mass deposition of this Co sample, 63.7 μg cm^{-2} (as determined by reference-free XRF, see below), was made available to all participants beforehand for optional calibration purposes
6	Type 2 (oxide)	**TiO_2**	17.49 nm	
7	Type 2 (oxide)	**TiO_2**	56.11 nm	
8	Type 2 (oxide)	**Al_2O_3**	131.41 nm	
9	Type 3 (multilayer)	**Ti/Ni/Mn**	230 nm/730 nm/140 nm	
10	Type 3 (multilayer)	**Ti/Mn/Ni**	135 nm/125 nm/690 nm	
11	Type 3 (multilayer)	**Cr/Cu/Co**	140 nm/670 nm/80 nm	
12	Type 3 (multilayer)	**Cr/Co/Cu**	140 nm/145 nm/770 nm	
13	Type 4 (alloy)	**$Cr_xCo_yCu_z$**	500 nm	Mass fractions: 13% Cr, 9% Co, 78% Cu
14	Type 4 (alloy)	**$Cr_xCo_yCu_z$**	1000 nm	Mass fractions: 11% Cr, 14% Co, 75% Cu
15	Type 4 (alloy)	**$Ti_xMn_yNi_z$**	500 nm	Mass fractions: 12% Ti, 12% Mn, 76% Ni
16	Type 4 (alloy)	**$Ti_xMn_yNi_z$**	1000 nm	Mass fractions: 8% Ti, 12% Mn, 80% Ni
17	Type 5 (LIB material)	**NMC622**	57 μm	

desired total thickness and respective mass fractions of the constituents. For such a deposition of a large number of these sublayers, the XRF measurements are only sensitive to the average composition of this quasi-alloy when taking secondary fluorescence effects into account, as can be shown experimentally.[7,23] Consequently, samples with almost arbitrary mass fractions can be designed and produced.

The single layers, alloys and multilayers containing manganese (Mn), nickel (Ni), titanium (Ti) and scandium (Sc) were fabricated by AXO DRESDEN. Fraunhofer IWS fabricated those with cobalt (Co), copper (Cu) and chromium (Cr) as well as the oxide layers. For both manufacturers, samples were deposited on 15.24 cm (6 in) silicon wafer substrates, with thicknesses between about 0.4 mm and 0.7 mm, that were cut to individual square pieces of 18 × 18 mm^2 using a wafer saw. Because of the exceptional lateral homogeneity of the deposition process and the silicon substrates, these individual pieces are assumed to be nominally identical in terms of their individual thicknesses and composition. This was verified for a low number of individual samples using lateral XRF scans in the SI (SI-4). The nominal values, *i.e.* target values of the deposition process, for thickness and composition are those given in Table 1.

Battery electrode material (type 5). Lithium-ion battery (LIB) electrode samples (sample #17) were produced in an in-house battery production line at the MEET Battery Research Center. The electrode paste consisted of 95% (mass fraction) cathode active material (NMC622, $LiNi_{0.6}Co_{0.2}Mn_{0.2}O_2$), 2% conductive carbon black and 3% binder (PVdF, polyvinylidene difluoride) with a solid content of 77% in *N*-methyl-2-pyrrolidone. After mixing, the paste was coated one-sided on aluminum foil (thickness 15 μm) with a mass loading of 13.5 mg cm^{-2} and dried at 100 °C. A porosity of 30% was achieved by calendering, resulting in a coating thickness of 57 μm. The electrode sheets were cut using ceramic cutting tools to produce samples of approximately 18 × 18 mm^2, which were distributed to the participants of the interlaboratory comparison.

Interlaboratory comparison

Participants of the interlaboratory comparison. Nine independent laboratories participated in the interlaboratory comparison. These included major XRF instrument manufacturers and other XRF specialists, listed here in alphabetical order.

- Bruker AXS – Advanced X-ray Solutions GmbH (Karlsruhe, Germany).
- Bruker Nano GmbH (Berlin, Germany).
- Fluxana GmbH & Co. KG (Bedburg-Hau, Germany).
- Helmut Fischer GmbH (Berlin, Germany).
- Hitachi High-Tech Analytical Science (Uedem, Germany).
- Physikalisch-Technische Bundesanstalt (Berlin, Germany).

- Rigaku (Takatsuki, Japan).
- Shimadzu (Kyoto, Japan).
- Spectro Analytical Instruments (Kleve, Germany).

All organizers of the interlaboratory comparison are authors of the present work. Organizers who also participated in the interlaboratory comparison are Physikalisch-Technsiche Bundesanstalt, Bruker Nano GmbH, and Helmut Fischer GmbH.

XRF measurements of the interlaboratory comparison. For the interlaboratory comparison, the participants were asked to perform XRF analysis of all 17 samples listed above without any sample preparation (for more details see the measurement protocol in SI-5). Almost all participants returned results for all samples, only two of the 17 samples were not measured by one participant (sample #8 and #17). All measurements were to be conducted according to predefined measurement instructions, which had been sent to all participants. This entailed performing the XRF analysis in conventional beam geometry as available to the individual instrument, avoiding grazing incidence conditions. Both energy-dispersive and wavelength-dispersive spectrometers were utilized. Measurements were to be conducted in the center of the sample, with 10 repeated measurements, each of which should contain a significant number of events to ensure and evaluate repeatability. Detailed description of the individual instruments will not be disclosed to preserve anonymity.

The participants were asked to provide results in the form of mass depositions (in μg cm^{-2}) for samples of type 1 to 4 and in terms of mass fraction (in %) for type 5, *i.e.* the LIB material NMC622. All measurements for the interlaboratory comparison were conducted during the second half of the year 2022 and results were anonymized by PTB.

Complementary measurements

Reference-free XRF analysis. All samples used for the interlaboratory comparison were analyzed using XRF by PTB. In contrast to all other participants, this method uses monochromatized synchrotron radiation and calibrated instrumentation to achieve results that are SI-traceable. Further details about this reference-free XRF method can be found elsewhere.[7,11,19] The results were handled and integrated into the interlaboratory comparison in the same manner as all other participants. To optimize the excitation conditions of each chemical element, measurements were performed at different beamlines providing different ranges of monochromatic photon energies: at the four-crystal monochromator beamline[24] and at the plane-grating monochromator beamline for undulator radiation,[25] both located in the PTB laboratory, and at the BAMline.[26] All three beamlines are located at the electron storage ring BESSY II. The end-stations used by PTB, including calibrated photodiodes, calibrated silicon-drift detectors, and a calibrated diaphragm, were employed in an equivalent way at all three beamlines. The beamlines have very different ranges of available monochromatic photon energies, in principle covering the complete range from about 79 eV to 60 keV.

The mass deposition of the Co layer (sample #5), as determined by this reference-free XRF approach (63.7 μg cm^{-2}), was given as reference value to all participants of the interlaboratory comparison beforehand, for optional calibration purposes.

X-ray reflectivity measurements. The thickness of layers in the nanometer range, and especially of multilayers, can be measured using X-ray reflectometry (XRR).[27] Monochromatic radiation from an X-ray source is reflected from the sample at varying grazing angles of incidence (from close to 0° to about 5°). The interference effects of the reflected rays lead to angle-dependent intensity minima and maxima, and these can be related to the thickness of the respective layers with picometer precision using the Bragg equation. The typical film thicknesses accessible with conventional laboratory X-ray sources are in the range of 1 nm to 200 nm when the substrate surface is sufficiently smooth (*i.e.* polished). Otherwise, the accuracy of the XRR measurements is significantly reduced due to diminished interference effects. Conversely, the roughness of the surface and interfaces, as well as the densities of the layers, can be determined, albeit within the limits of the fit model's validity. Here we used an in-house developed XRR system in a symmetric goniometer geometry (θ/θ) using Cu Kα radiation (8.0 keV). A twin mirror arrangement consisting of parallel beam Göbel mirrors in the source and the detection channels provides an instrumental resolution of better than about 0.03° (FWHM).

As it is not possible to measure the film thickness *in situ* during the sputtering process, in most cases several test samples were coated and measured with XRR in order to iteratively adjust the sputtering parameters until the target values were achieved. Once these parameters have been established, the precision, stability and reproducibility of the coating process routinely allow many nominally identical samples and samples with large, coated areas to be produced.

Lateral homogeneity assessment of LIB material by micro-XRF analysis. The lateral homogeneity of the LIB material (NMC622) coated on aluminum foils was analyzed by Bruker using the micro-XRF analyzer M4 TORNADO plus (Bruker Corporation, Billerica, MA, USA). The fast mapping of two samples was performed under the following experimental conditions: a microfocus X-ray tube with Rh target was used, its high voltage was 50 kV. The X-ray lens had a focal spot of <20 μm for Mo-Ka. No primary filter was used. Two 60 mm^2 silicon drift detectors with resolution <140 eV for Mn Ka were available and the chamber pressure was 20 mbar. The mapping was performed with a step size of 20 μm. The elemental composition distribution was calculated for the measured maps using a standard FP-based quantification model. A fixed percentage of LiO_2 oxide (75% atomic fraction) was assumed.

X-ray tomography. X-ray absorption and tomography experiments on the LIB material NMC622 (sample #17) were performed by HZB at the BAMline imaging end-station at the BESSY II synchrotron to characterize and confirm its spatial homogeneity.[28,29] For sample preparation, a 1 mm wide part of the 18 × 18 mm^2 electrode material was cut out and mechanically fixed between two polished poly(methyl methacrylate) (PMMA) rods to maintain a flat geometry and to avoid adhesives or resins that could distort the local absorption measurements. This design allowed for height dependent analysis of radial variations in absorption within the sample. Synchrotron X-ray

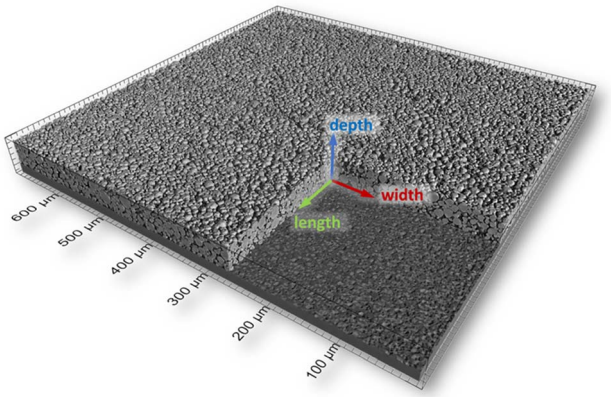

Fig. 1 3D rendering of a part of the reconstructed volume of the LIB NMC622 sample.

transmission experiments were performed at a photon energy of 30 keV using the W/Si double-multilayer monochromator with an energy resolution of $\Delta E/E = 4.3\%$.[28] The choice of 30 keV was based on preliminary tests showing optimal transmission and contrast for the highly absorbing NMC622 active material (95% mass fraction in the cathode composite), which was essential to ensure measurable transmission through the 1 mm cutout of the prepared sample. Tomographic scans were acquired in continuous fly-scan mode with 2500 projections over 180°, each with 0.4 s exposure time. The synchrotron beam was converted to visible light using a $CdWO_4$ scintillator coupled with magnifying optics, achieving an effective pixel size of 0.36 µm and yielding an effective resolution between about 0.8 µm and 1 µm. Image reconstruction as shown in Fig. 1 employed filtered back-projection.

Depth profiling. Time-of-flight secondary ion mass spectrometry (ToF-SIMS) was performed to investigate aging effects of the samples and potential interface diffusion. ToF-SIMS is a state-of-the-art surface analysis technology that is widely used for the analysis of thin films of oxides, multilayers, alloys, and battery materials.[30] The method has an extremely high surface sensitivity: it probes the outermost 1 to 3 atomic layers. Furthermore, the time-of-flight mass analyzer has the capacity to detect all different masses simultaneously with high mass resolution. In imaging mode, chemical maps can be obtained with a lateral resolution of less than 100 nm. In depth profiling mode, a depth resolution of approximately 1 nm can be achieved.

The ToF-SIMS measurements were performed using a ToF-SIMS 5 (IONTOF, Münster, Germany) on a selected number of representative samples of the interlaboratory comparison. The instrument was equipped with a Bi-liquid metal ion source as the analysis ion gun. An additional dual beam source was installed to provide O^+ and Cs^+ ions for the sample erosion for depth profiling. Static SIMS spectra and surface images were acquired with primary ions (Bi^+) at a beam energy of 25 keV in both positive and negative secondary ion polarity. Depth profiles were acquired in both polarities. Samples were sputtered with O^+ ions at an energy of 1 keV in the positive polarity mode and with Cs^+-ions at an energy of 1 keV in the negative polarity mode.

Gravimetric determination of mass depositions. As an independent method that can be used to verify XRF results, a gravimetric determination of the mass deposition per unit area (m A^{-1}) was also performed. This involved measuring the mass (m) and area (A) for selected samples to demonstrate this method's capabilities for samples like those used in the interlaboratory comparison. Gravimetric measurements were based on a dedicated high precision balance and a digital microscope. Uncoated wafer substrates were weighed before the actual deposition process and again after the thin film deposition. From the difference in weight the total mass m deposited can be derived. This approach allows direct comparison with the results of XRF analysis, which determines the elemental mass deposition of individual chemical elements $(\text{m A}^{-1})_i$. Helmut Fischer GmbH holds an accreditation certificate[31] issued by the German accreditation body DAkks, that covers the measurement of mass per unit area of thin foils. The individual measurements performed in the present work were carried out according to this accreditation, with the added step of subtracting the mass of the wafer substrate from the total mass after deposition, resulting in the mass of the actual thin film deposition. For direct comparison and cross-evaluation of the analytical performance, XRF measurements were realized on the same samples using a commercially available micro-XRF bench-top instrument (Fischerscope; Helmut Fischer GmbH, Sindelfingen, Germany) equipped with a 50 kV X-ray tube.

Results and discussion

Results of complementary measurements

Reference-free XRF analysis. All the results of the reference-free XRF measurements by PTB were included in the interlaboratory comparison. Since most of the samples used in the interlaboratory comparison contain significant amounts of

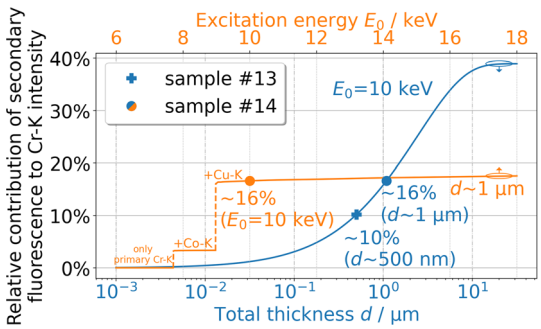

Fig. 2 Calculated relative contributions of the secondary fluorescence effect to the total XRF intensity of Cr is shown for alloys consisting of Cr, Co and Cu, with exemplary weight fractions of samples #14 (sample #13 is similar). The influence of both varying layer thicknesses (blue curve, bottom abscissa) and varying photon energies of the excitation (orange curve, top abscissa) is shown. Elliptical markers indicate the corresponding abscissa for each curve.

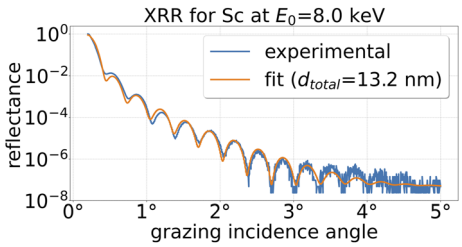

Fig. 3 XRR result for the Sc single layer with a thickness of about 13.2 nm (sample #1), measured at a photon energy of approximately 8.0 keV.

more than one chemical element, the analysis of these samples requires accurate consideration of the secondary fluorescence effect. This is because X-ray fluorescence radiation from one element may have enough energy to induce X-ray fluorescence radiation from another element. This effect may have a relative contribution of several tens of percent, but of course, is strongly dependent on the actual measurement conditions and details of the sample: Fig. 2 shows that for very thin samples (here below ~100 nm for CrCoCu alloys) the contribution of this secondary effect essentially vanishes (blue curve). While it can rise to over 35% for bulk samples, for the samples in the present work the contributions were in the range of about 10% to 20%. Specifically, while sample #13 (plus symbol in Fig. 2, 500 nm CrCoCu alloy) has a relative contribution of about 10% to its Cr signal intensity, sample #14 (circle symbol in Fig. 2, 1000 nm CrCoCu alloy) has a relative contribution of about 16%. While the effect also depends on various experimental and analytical details and may therefore vary between different setups, it can only be avoided if the X-ray excitation is tuned below the respective K edges of the enhancing elements (orange curve of Fig. 2). For the reference-free XRF quantification, such an experiment was performed, and the corresponding analytical results using monochromatic X-ray radiation with photon energies above and below the edge were in good agreement with each other (within <2%).

X-ray reflectivity measurements. Samples coated by AXO DRESDEN and Fraunhofer IWS were characterized by XRR to determine deposition rates. Results of the total deposition thickness values are listed in Table 1. In principle, the mass deposition (g cm^{-2}) accessible with XRF can be converted into thickness values (nm), as measured with XRR, by dividing the mass deposition by the density of the layer (g cm^{-3}), which usually is taken from literature. However, thin layers in the nano-regime produced by sputter deposition can exhibit deviations from tabulated bulk densities, for example, due to the growth process itself or due to ambient oxidation. Thus, density was a fitting parameter in the evaluation of the experimental XRR data. One such example are the Sc samples (#1 to #3): Fig. 3

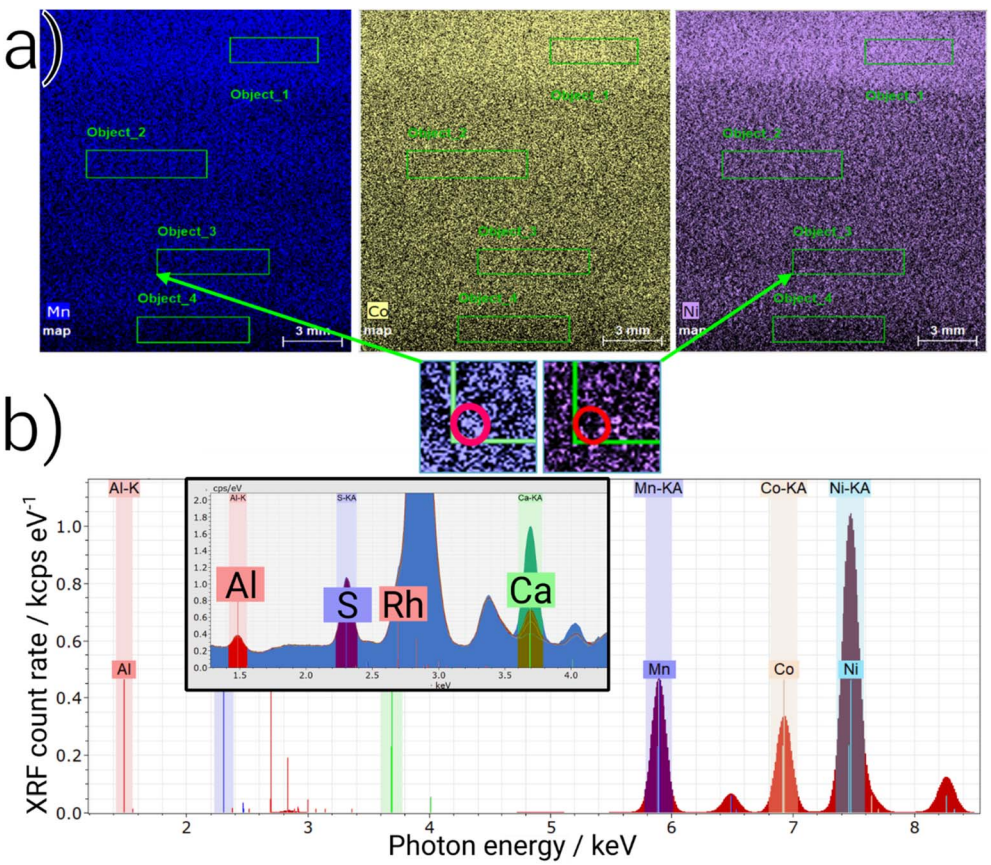

Fig. 4 (a) Element distribution over the LIB (NMC622) surface, with the micro-XRF intensity color-coded for Mn (blue), Co (yellow) and Ni (purple), linearly scaled across the individual dataset range given in the main text. The spot size of the inset maps is about 500 µm. (b) Average micro-XRF spectrum of the LIB sample; the inset shows very low contaminations of Al, S and Ca.

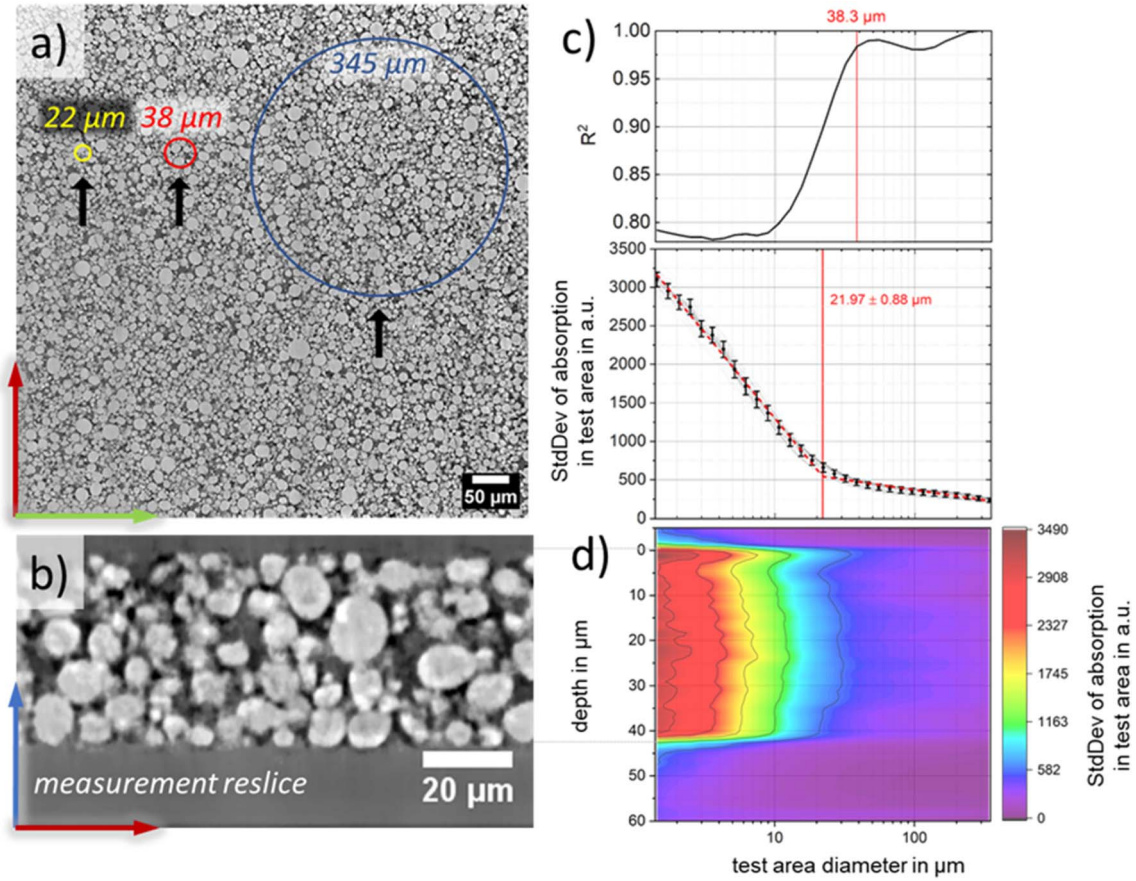

Fig. 5 Spatial homogeneity analysis of the LIB material using X-ray tomography: (a) cross section in the width-length direction showing selected investigation area sizes (yellow, red and blue circle), (b) cross section in width-depth direction, (c) plot of area-size dependent standard deviation (StdDev) and coefficient of determination (R^2). For the StdDev of the absorption a segmented regression fit was conducted, with two segments of the fit crossing at (21.97 ± 0.88) µm, as indicated by the red line. For the coefficient of determination, a qualitative difference below a diameter of approximately 38.3 µm can be observed. (d) Related depth-dependent standard deviation. Note that the horizontal axis is plotted on a logarithmic scale.

shows an exemplary XRR curve for sample #1. Although the fit model includes an additional native Sc oxide layer and can largely describe the measured oscillations, the deviation to the experimental data is greater than that observed for any of the other pure elements. However, the XRF measurements presented in this work are not sensitive to such a native oxide layer, so they may not be as comparable to the XRR results as they generally are.[32] Nevertheless, the nominal values of the samples (as determined by XRR) are included in the results of the XRF interlaboratory comparison given below for context.

Lateral homogeneity assessment of LIB material by micro-XRF analysis. Fig. 4a shows the elemental map distribution with regards to Mn, Co and Ni of the LIB material NMC622 (sample #17). In addition, Fig. 4b shows the average micro-XRF spectrum of this sample. As expected from the production process, the coating exhibits compositional heterogeneity in the lateral distribution of the elements at the microscopic (sub-millimeter) scale, with particle sizes up to several dozen micrometers. That is best seen in the inset distribution maps for Ni and Mn. Generally, the lateral distribution of the main coating elements is sufficiently homogeneous on the macroscopic scale (centimeter): these lateral variations of the observed XRF intensities that are visible in Fig. 4a do not exceed 2.5% for Co, 2.2% for Mn and 2.9% for Ni. The coating thickness can also be derived from these measurements, and its average is typically about 100 µm, with a spread of less than 0.1%. The absolute variation of the element concentrations, calculated for four selected locations (green rectangles in Fig. 4a with a size of about 5 mm^2), is less than 0.02 wt% for the three main elements. However, some spots have been observed to reach up to 150 µm coating thickness. It should be noted that the minimal spot size that was recommended for the participants of the interlaboratory comparison was 150 µm. This means that any heterogeneity at lateral scales below this size should not have any impact on the results of the interlaboratory comparison. In addition, XRF lines of some contaminating light elements – Al, S and Ca – were observed in the average map spectrum, *cf.* Fig. 4b. The trace amounts of these light elements are also not expected to influence the quantitative results of the interlaboratory comparison.

X-ray tomography. X-ray tomography measurements were performed to investigate the length scale of heterogeneity in the

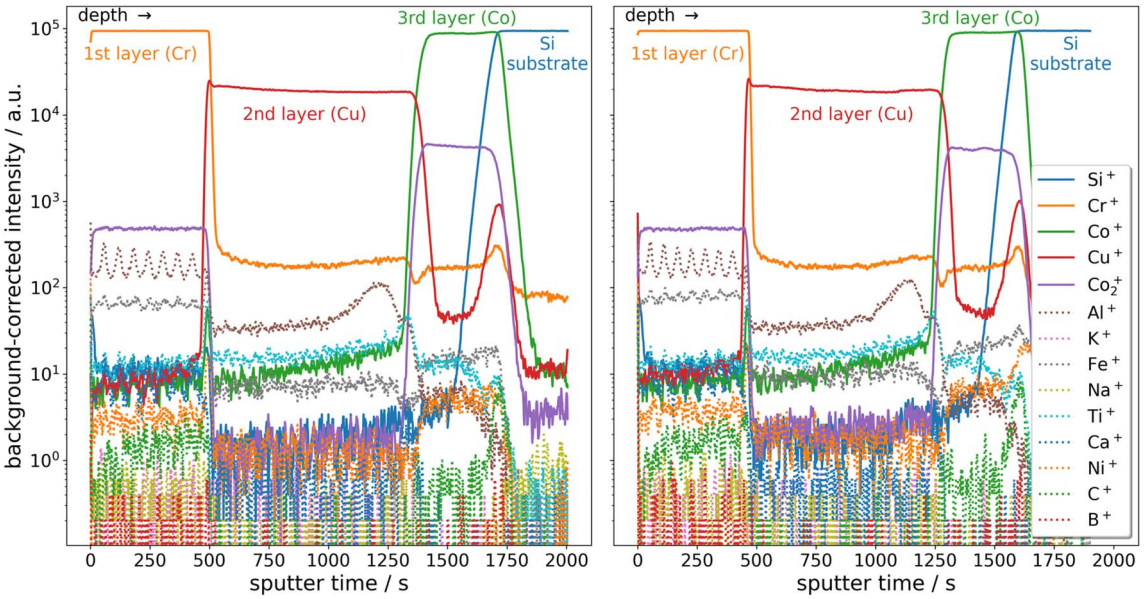

Fig. 6 ToF-SIMS depth profiles of sample #11 (Cr/Cu/Co multilayer) after different storage periods, showing the depth distribution of several elements/ions. The figure on the right shows data from nine months after the left figure. The three main layers can clearly be identified (solid lines). Due to the high sensitivity of ToF-SIMS, trace elements and minor impurities can be detected at low intensities in the layers and interfaces (dotted lines), but these are not relevant for the subsequent interlaboratory comparison using XRF.

LIB material NMC622 (sample #17) further: a systematic procedure was developed to determine the smallest radial diameter of an analyzed region where the average absorption coefficient becomes effectively independent of local positioning on the sample, as shown in Fig. 5a. For this, the average absorption per area was measured over a raster covering the entire region of interest and across all reconstructed slices. The standard deviation of the absorption coefficient was evaluated as a function of both the analyzed diameter with respect to the sample surface and the sample height. The values of the standard deviation of the absorption coefficients were fitted with two linear functions as shown in Fig. 5c. Analysis of this fit in terms of its coefficient of determination R^2 revealed that localization effects, *i.e.* significant position-dependent variations, start to emerge below a diameter of approximately 38.3 μm. The investigation also showed that the homogeneity is depth dependent, see Fig. 5d. The uppermost layers of the LIB material are found to be slightly less homogeneous, likely due to the calendering process and the forces involved therein that may induce material changes.[33] Consequently, the material is well suited for XRF analysis in the interlaboratory comparison, which is mostly based on beam spots and thus lateral averaging in the range of several hundred micrometers and a depth of information of several micrometers. This corroborates the results of the micro-XRF analysis.

ToF-SIMS depth profiling. Direct comparison of the ToF-SIMS measurements taken nine months apart revealed no significant changes in the samples investigated, both for the surface (spectrometry and imaging) and for the depth profile (layer sequence, layer composition, contamination). Fig. 6 shows an example of a comparison of depth profiles for sample #11, which revealed no significant differences: the layer structure of the reference samples is stable over a period of at least nine months. Furthermore, no significant interdiffusion occurred between the nominally separate layers, and contaminations were only observed in a negligible amount. It should be noted that, while the three main constituents of sample #11 (Cr, Cu, Co) can be observed outside of their respective nominal layers (see Fig. 6), this fraction only amounts to less than 0.5% each. Based on these results, no limitations to their use as reference samples or their use in the interlaboratory comparison were identified.

Table 2 Comparison of gravimetric results and XRF results with regard to the mass deposition per unit area of the deposited Ni thin films

Nominal Ni thickness/nm	Total mass m deposited/μg	Total area A of deposition/cm	Gravimetrically determined mass deposition per unit area (m A^{-1})/μg cm^{-2}	Mass deposition per unit area as determined by XRF/μg cm^{-2}
5	15.6 (75)	3.1855 (5)	5 (3)	4.3 (2)
15	41.6 (75)	3.1806 (5)	13 (3)	13.6 (3)
50	143.4 (75)	3.1738 (5)	45 (3)	45.7 (6)
150	423.8 (75)	3.1770 (5)	133 (3)	134.7 (10)
0 (blank)	0.0 (75)	3.1787 (5)	0 (3)	0.00 (5)

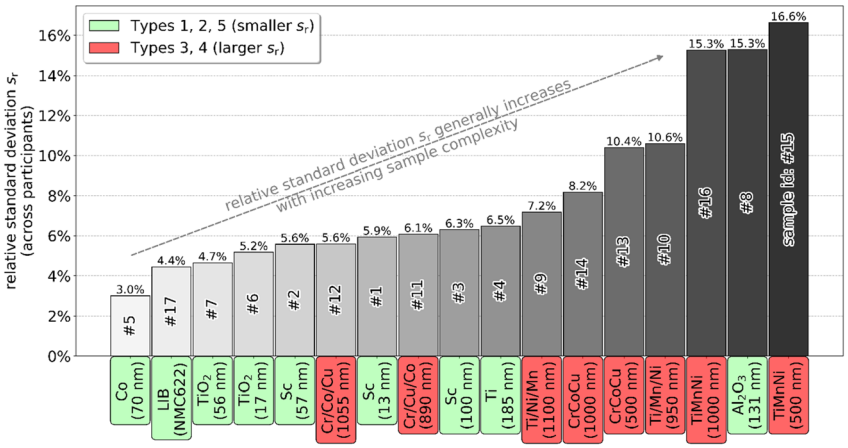

Fig. 7 Relative standard deviation s_r for each of the 17 samples across all participants. For samples with multiple results (*e.g.* the LIB material with three individual results for three different chemical elements), the maximum deviation was selected. In general, samples from types 3 and 4 (*i.e.* multilayers and alloys) show larger relative standard deviations.

Gravimetric determination of mass depositions. Prior to thin film deposition, a set of five uncoated wafer substrates that were not used for the interlaboratory comparison were weighed, with each substrate having a mass of approximately 470 mg. Four of these wafers were then coated with a thin film of Ni. The film thicknesses targeted for deposition were 5 nm, 15 nm, 50 nm and 150 nm, respectively. One uncoated wafer was used as a blank reference, which remained uncoated but was treated in the same way as the others in order to study systematic changes in the substrates not related to the deposition process. After the deposition process, all five samples were reweighed, and the area of deposition was measured using a digital microscope. The results of these measurements are summarized in the following Table 2. The mass deposition of each coating was in the range of a few tens to a few hundred µg, accounting for as little as about 0.003% of the total mass of the coated wafers. Consequently, the uncertainty of the final gravimetric results is dominated by that of the weighting process.

A comparison of the gravimetric and XRF results reveals that, given the respective uncertainties, they are equivalent in terms of mass deposition per unit area. This demonstrates that determining mass and area individually is equivalent to determining mass deposition per unit area directly. In principle, this could be used to verify the deposition rates used in producing the thin films independently.

Results of interlaboratory comparison

Below, a summary of the results of the interlaboratory comparison is presented, and a principal component analysis is

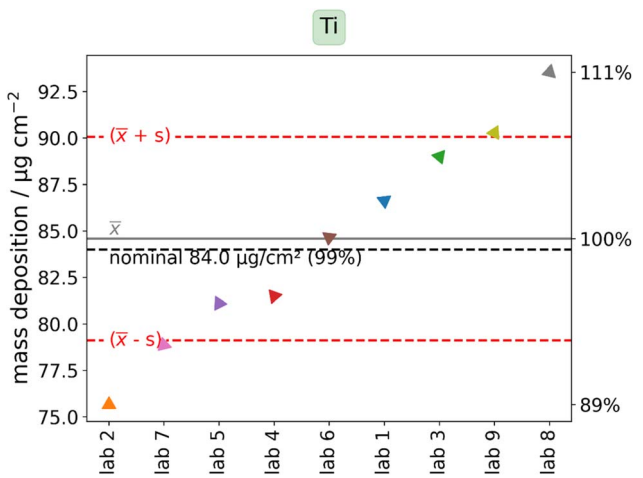

Fig. 8 Individual results of all 9 participants for the pure Ti layer (sample #4). The targeted mass deposition was 84 µg cm^{-2} as indicated by the dashed black line. The mean value $\bar{x}$ of the results (solid grey line) and the interval defined by the standard deviation s (dashed red lines) are indicated for the purpose of clarity. The maximum relative deviation is about 11% in comparison to the mean value. Results for sample type 2 (oxides).

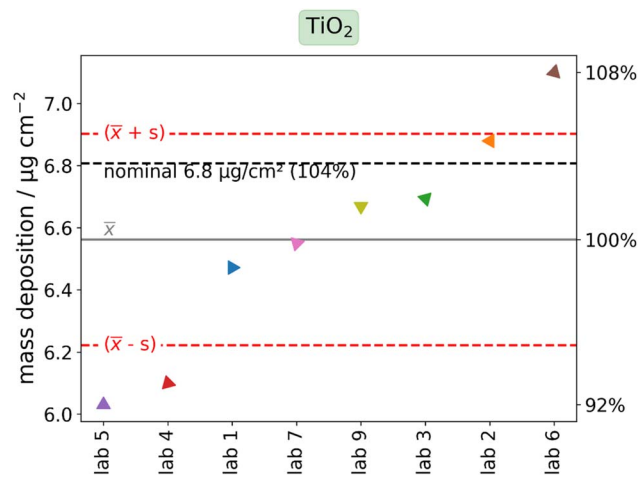

Fig. 9 Individual results of 8 out of 9 participants for the TiO_2 layer (sample #6). One laboratory (lab 8) did not submit any data for this sample. The targeted mass deposition was 6.8 µg cm^{-2} as indicated by the dashed black line. The mean value $\bar{x}$ of the results (solid grey line) and the interval defined by the standard deviation s (dashed red lines) are indicated for the purpose of clarity. The maximum relative deviation is about 8% in comparison to the mean value.

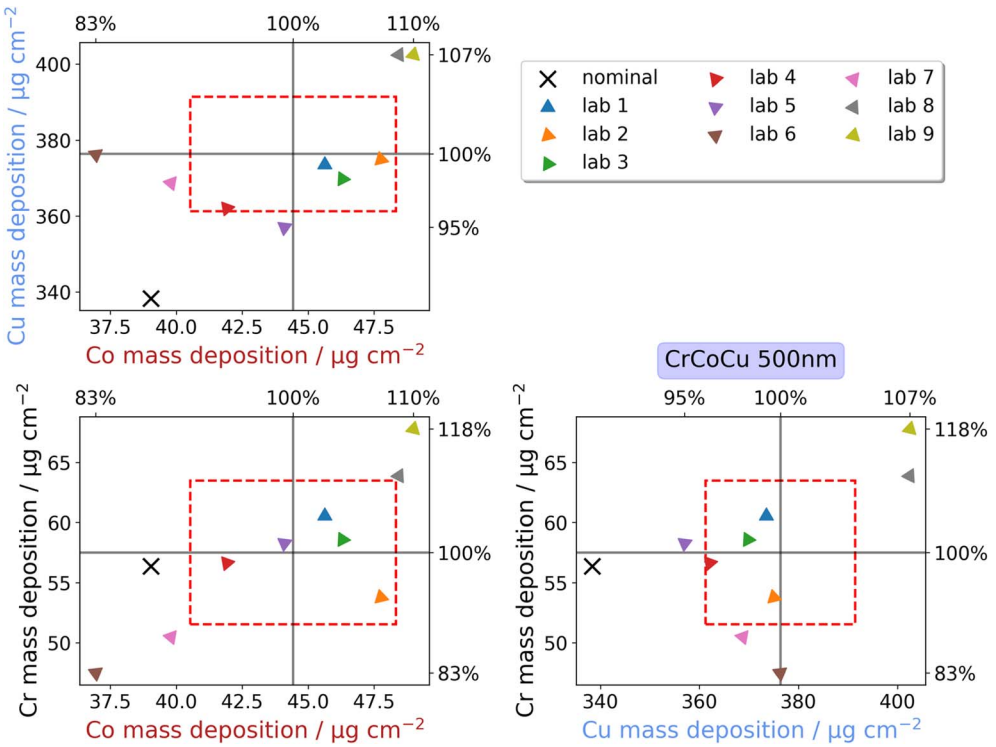

Fig. 10 Individual results of all participants for the alloy containing Cr, Co, and Cu (sample #13). The participants reported three individual results, *i.e.* the element-specific mass depositions of Cr, Co, and Cu, which are compared in a three-way manner here (triangle symbols). The targeted mass deposition is indicated by black crosses. The mean values of the results (solid grey line) and the interval defined by the standard deviation (dashed red lines) are indicated for the purpose of clarity. The maximum relative deviation is about 18% in comparison to the mean value.

performed to provide a more detailed interpretation of the results. The comprehensive lists of all individual results of the present interlaboratory comparison can be found in the SI (SI-2). Here, for the sake of clarity, we limit ourselves to discussing selected results and provide an overall interpretation. Fig. 7 shows the relative standard deviation of the quantitative results for each of the 17 samples across all participants. In summary, while the results of most samples show a relative standard deviation well below 10%, samples of types 3 and 4 – multilayers and alloys with multiple elements and a significant secondary fluorescence effect – tend to show greater deviation, whereas single-element layers tend to show somewhat lower deviation. As the individual results were not provided with uncertainty values by the participants, these relative standard deviation values can be used to estimate the general XRF uncertainty. Some additional individual results are discussed below.

Selected individual results of interlaboratory comparison

Results for sample type 1 (single-element layer). Fig. 8 shows the results for the pure Ti sample (sample #4) of sample type 1. Participants were asked to provide elemental mass deposition values (in g cm^{-2}). The relative standard deviation over all participants is about 6% for this example and for all samples in this sample type category, except for the Co sample, which has a relative spread of about only 3%. This may indicate that the Co mass deposition determined by reference-free XRF, which was made available to all participants in advance, might have been used to pre-calibrate at least some of the participants' XRF instruments, as was suggested but not enforced. The overall consistently low standard deviation for the sample type 1 category provides evidence of the generally good precision and accuracy achievable for single-element layers with XRF instruments as used by the independent participants.

As in this case, and for almost all the type 1 samples, the nominal mass depositions are very close to the mean of the participants (within a single percentage point). This is in line with the expectation that for single layers that can be deposited in a straightforward manner, the calibration of the sputtering rates can be controlled well. The only exception is the scandium sample with the lowest mass deposition of all samples (#1), for which the nominal value is about 14% higher than the mean value, corresponding to a difference of about 1 nm in film thickness out of a total of ~12 nm. This is most likely due to the oxidation of the Sc films, as discussed above, since no capping layer was used. Additionally, nonlinear deposition kinetics of Sc at the beginning of the deposition process, compared to later stages when more material is already deposited (see for example[20]), could have an impact.

Fig. 9 shows an example result for one of the TiO_2 samples (sample #6) of sample type 2. Participants were asked to give the total mass deposition values for the oxide layers based on stoichiometric composition (in g cm^{-2}). The relative standard deviation over all participants is about 5% for both TiO_2 samples in this sample type category, very similar to the single-

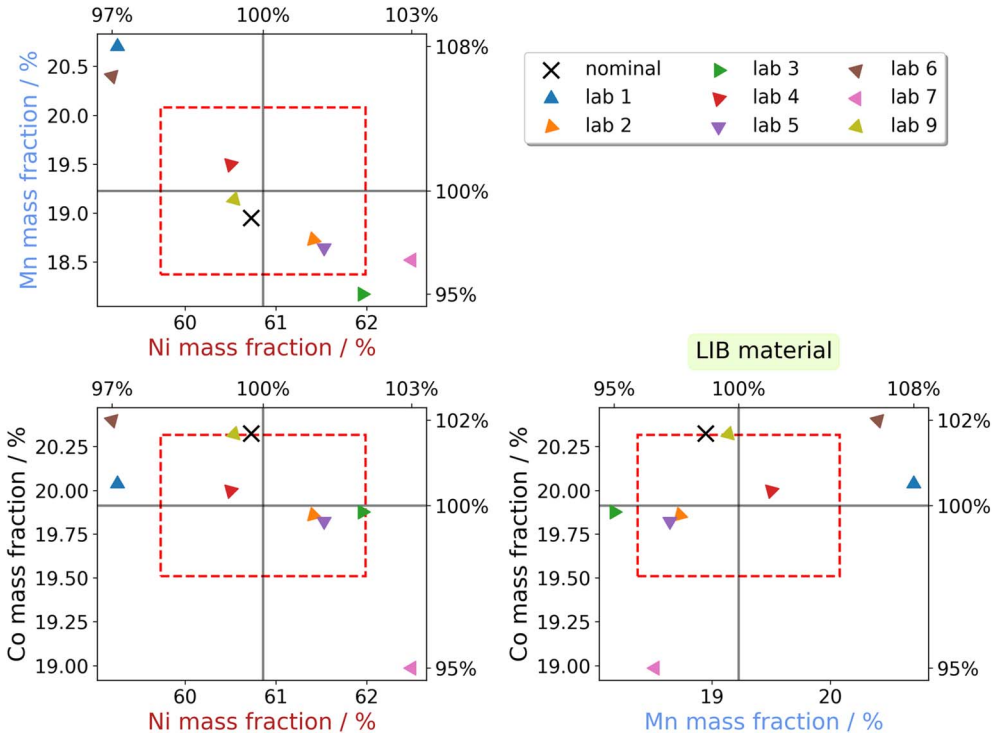

Fig. 11 Individual results of 8 out of 9 participants for the LIB material NMC622 (sample #17). One laboratory (lab 8) did not submit any data for this sample. The participants reported three individual results, *i.e.* the element-specific mass fractions of Co, Ni, and Mn, which are compared in a three-way manner here (triangle symbols). The targeted mass fractions of NMC622 are indicated by black crosses. The mean values of the results (solid grey line) and the interval defined by the standard deviation (dashed red lines) are indicated for the purpose of clarity. The maximum relative deviation is about 8% in comparison to the mean value.

layer results in type 1, demonstrating that such metal oxides can also be easily quantified with relatively good accuracy and precision.

The relative standard deviation for the Al_2O_3 sample is considerably higher at 15%. This might indicate that although the low-Z element aluminum ($Z = 13$) can be detected by most general purpose instruments, *i.e.* devices not necessarily optimized for the detection of light elements, the absorption of its X-ray fluorescence radiation in air is already significant and impacts the accuracy of the results: about 77% of the aluminum K radiation is absorbed in 1 cm air. While this attenuation can in principle be taken into account, it is subject to an increased uncertainty contribution if it is not determined in dedicated experiments.[34]

The nominal mass depositions for the three oxides do not deviate by more than 6% from the mean of the participants, confirming that the deposition process of these stoichiometric oxides can be controlled with a high degree of precision, as would be expected from the results of sample type 1.

Results for sample type 3 and 4 (multilayers and alloys). Fig. 10 shows an example result for one of the alloys containing Cr, Co, and Cu (sample #13) of sample type 4. Participants were asked to provide elemental mass deposition values of the three main constituents in g cm^{-2} (*i.e.* Cr, Co, and Cu in the example). The relative standard deviation of these results is about 8% when averaged over the three chemical elements, with both the lower-concentration elements, Cr and Co, whose XRF signals are enhanced by the XRF radiation of the heavier Cu, showing more than twice the inter-participant variation as Cu (about 10% *vs.* 4%). Similar trends can be seen for all 8 samples in these two sample type categories, which show the greatest variation between participants overall. Looking at the maximum standard deviation of the results for each of the three elements, and then averaging over all participants, reveals relative standard deviations ranging from about 6% to about 17% for samples in this sample category, with the majority below 11%. The largest deviation can be seen for the two alloys containing Ti, Mn, and Ni (about 15% for Ti in sample #16 and 17% for Ti in #15). These larger deviations are expected to be due to the increased complexity of these sample categories compared to the thin single-layer samples and oxides: according to the design objective, the influence of the secondary fluorescence effect is of the order of about 10% for all samples in category 3 & 4. Moreover, the increased layer thickness means that absorption effects play a greater role and could be an additional source of variation.

Results for sample type 5 (LIB material NMC622). Fig. 11 shows the results for the LIB material NMC622 (sample #17) of sample type 5. In contrast to the mass depositions (in g cm^{-2}) requested for the samples in types 1 to 4, participants were asked to provide the elemental mass fractions of Ni, Co, and Mn for this bulk material. The relative standard deviation of these results averaged over the three chemical elements is only about 3%, making it one of the results with the lowest variations

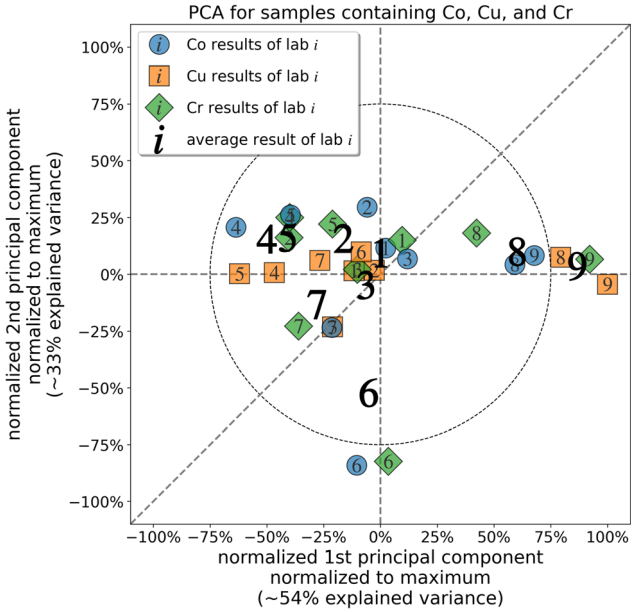

Fig. 12 Principal component analysis of samples #11–14, which contain Co, Cu, and Cr. Only the first two principal components are shown. The averages for individual laboratories are indicated as large numbers.

between participants. More specifically, the relative standard deviations for Ni and Co are about 2%. However, for Mn they are about twice as high at 4%. Here, Mn receives a substantial XRF enhancement due to the secondary fluorescence effect (20% or more), demonstrating that handling this nonlinear effect plays a critical role in the accuracy of the analytical results. The smaller deviations observed for these results, compared to those of category 3 & 4 (multilayers and alloys), may indicate that bulk materials are analytically easier to treat. In the bulk sample, elemental mass fractions are determined on a relative scale, which are independent of sample thickness, whereas category 3 & 4 require quantification of absolute mass depositions.

Principal component analysis. Since the interlaboratory comparison encompasses a rather large number of data points (9 participants, 17 samples, most samples with more than one chemical element), it can be helpful to reduce the dimensionality of the data set, for example, with a principal component analysis (PCA). The samples in category 3 (multilayers) were designed to contain the same chemical elements as the equivalent samples in category 4 (alloy). This approach may therefore reveal multivariate relationships between them. Here, we utilize TensorLy[35] for the PCA, which is based on a Tucker decomposition.[36] Fig. 12 shows the results of such a PCA performed on the data of all samples containing Co, Cu, and Cr (*i.e.* samples #11 to 14). A direct visual comparison of the individual average results shows that laboratories 1 to 5 and 7, laboratory 6, and laboratories 8 to 9 form distinct clusters. This suggests that laboratories 6, 8 and 9 consistently produce different quantitative results compared to the other participants, particularly with regard to Co, Cu and Cr. In fact, laboratories 8 and 9 produced overestimates for all four samples, compared with the mean result for all participants. Conversely, laboratory 6 produced overestimated results for the multilayers (sample #11 to 12) and underestimates for the alloys (sample #13 to 14). The results for Cu are qualitatively different from those for Co and Cr. Quantitatively, they show consistently smaller relative deviations. For example, by a factor of about 1/2 for sample #13. This is most likely because Cu has the largest mass deposition of the samples compared and its X-ray fluorescence intensity is unaffected by the secondary fluorescence effect. Another PCA, with similar, although slightly less pronounced, results, is provided in the SI (SI-3) for samples #9 to 10 and #15 to 16, which contain Mn, Ni, and Ti. None of the participating laboratories only overestimates or underestimates all results of all samples. These results highlight the importance of investigating and assessing a large number of parameters (in this case, with changing chemical elements and sample complexity) to enable a more robust comparison.

Conclusion

We have presented the results of designing, producing, and pre-characterizing a rather large set of 17 sample sets of 5 different thin film categories that were used in an interlaboratory comparison for XRF. Although there are some element- and sample-specific differences between the results of the participating laboratories, there is generally good agreement between all participants for most of the results. It is neither possible nor worthwhile to clearly isolate the exact cause of the observed deviations from such an interlaboratory comparison, as it can only compare a limited number of different sample parameters. Details of individual instruments are generally proprietary and not available for comparison, so can only be examined indirectly. Moreover, the rather complex XRF analysis is influenced by many aspects and is often automated, and not necessarily adjusted for each measurement campaign: these aspects range from the fundamental atomic parameters used, instrument pre-calibration, spectral deconvolution approach, quantification scheme, and even simple operator errors. While the complexity of the presented interlaboratory comparison ultimately demonstrates the flexibility of the sample production methodology and the XRF method, there still seems to be a need to standardize such measurements to improve the comparability of analytical performance. This is especially true for thin film alloys, where the largest deviations between participants were observed and no appropriate standard exists. Currently, the authors of the interlaboratory comparison have started work on a German normative document (DIN/TS) in this respect.

Finally, we have shown that gravimetric quantification of thin films comprising as little as 0.003% of the total wafer mass can be performed reliably and with low uncertainties using a conceptually straightforward approach. Although gravimetry provides no information on individual elements, it can offer an independent measurement of the total mass deposition to validate XRF characterizations of thin films.

Author contributions

A. W.: data curation, formal analysis, investigation, methodology, project administration, software, validation, visualization, writing – original draft. C. S.: conceptualization, funding acquisition, methodology, project administration, writing – review and editing. Y. P. S.: resources, writing – review and editing. S. N. and B. H.: conceptualization, funding acquisition, methodology, resources, writing – review and editing. M. O.: data curation, formal analysis, investigation, methodology, visualization, writing – review and editing. I. M. and L. A.: funding acquisition, resources. M. F.: data curation, formal analysis, investigation, methodology, validation, writing – review and editing. R. U.: data curation, formal analysis, investigation, methodology, project administration, validation, writing – review and editing. M. W.: data curation, formal analysis, investigation, methodology, writing – review and editing. M. K. and P. G.: conceptualization, data curation, formal analysis, funding acquisition, investigation, methodology, resources, validation, writing – review and editing. E. B.: data curation, formal analysis, investigation, methodology, resources, validation, writing – review and editing. B. B.: conceptualization, funding acquisition, methodology, project administration, resources, supervision, writing – review and editing.

Conflicts of interest

There are no conflicts to declare.

Data availability

The data supporting this article have been included as part of the supplementary information (SI). Supplementary information is available. See DOI: https://doi.org/10.1039/d5ja00460h.

Acknowledgements

This work was supported by the WIPANO project under the grant "KALIB-RFA". The financial support of the WIPANO program is gratefully acknowledged. It is funded by the German Bundesministerium für Wirtschaft und Energie. The authors would like to thank all volunteer participants of the inter-laboratory comparison.

References

1 C. Vanhoof, A. Cross, U. E. A. Fittschen and L. Vincze, Atomic spectrometry update: review of advances in X-ray fluorescence spectrometry, *J. Anal. At. Spectrom.*, 2025, **40**, 2275–2289, DOI: 10.1039/D5JA90030A.

2 J. Sherman, The theoretical derivation of fluorescent X-ray intensities from mixtures, *Spectrochim. Acta*, 1955, **7**, 283–306, DOI: 10.1016/0371-1951(55)80041-0.

3 R. E. Van Grieken and A. A. Markowicz, *Handbook of X-ray Spectrometry, Second Edition. Rev. And Expanded*, CRC Press, New York, N.Y, 2001.

4 B. Beckhoff, *Handbook of Practical X-Ray Fluorescence Analysis*, Springer Berlin/Heidelberg, Berlin, Heidelberg, 2006.

5 D. K. G. De Boer, Calculation of x-ray fluorescence intensities from bulk and multilayer samples, *X-Ray Spectrom.*, 1990, **19**, 145–154, DOI: 10.1002/xrs.1300190312.

6 T. Shiraiwa and N. Fujino, Theoretical Calculation of Fluorescent X-Ray Intensities in Fluorescent X-Ray Spectrochemical Analysis, *Jpn. J. Appl. Phys.*, 1966, **5**, 886–899, DOI: 10.1143/JJAP.5.886.

7 A. Wählisch, C. Streeck, P. Hönicke and B. Beckhoff, Validation of secondary fluorescence excitation in quantitative X-ray fluorescence analysis of thin alloy films, *J. Anal. At. Spectrom.*, 2020, **35**, 1664–1670, DOI: 10.1039/D0JA00171F.

8 W. K. De Jongh, X-ray fluorescence analysis applying theoretical matrix corrections. Stainless steel, *X-Ray Spectrom.*, 1973, **2**, 151–158, DOI: 10.1002/xrs.1300020404.

9 I. M. Alarifi, Advanced selection materials in solar cell efficiency and their properties - A comprehensive review, *Mater. Today: Proc.*, 2023, **81**, 403–414, DOI: 10.1016/j.matpr.2021.03.427.

10 L. Zhou, K. Zhang, Z. Hu, Z. Tao, L. Mai, Y.-M. Kang, S.-L. Chou and J. Chen, Recent Developments on and Prospects for Electrode Materials with Hierarchical Structures for Lithium-Ion Batteries, *Adv. Energy Mater.*, 2018, **8**, 1701415, DOI: 10.1002/aenm.201701415.

11 B. Beckhoff, Traceable Characterization of Nanomaterials by X-ray Spectrometry Using Calibrated Instrumentation, *Nanomaterials*, 2022, **12**, 2255, DOI: 10.3390/nano12132255.

12 Federal Institute for Materials Research and Testing (BAM), *Nanoscaled Reference Materials*, https://www.nano-refmat.bam.de/en/, accessed 3 March 2026.

13 International Organization for Standardization (ISO), *Statistical Methods for Use in Proficiency Testing by Interlaboratory Comparison*, (ISO 13528:2022), 2022.

14 International Organization for Standardization (ISO) and International Electrotechnical Commission (IEC), *Conformity Assessment — General Requirements for the Competence of Proficiency Testing Providers*, (ISO/IEC 17043:2023), 2023.

15 E. Hund, D. L. Massart and J. Smeyers-Verbeke, Inter-laboratory studies in analytical chemistry, *Anal. Chim. Acta*, 2000, **423**, 145–165, DOI: 10.1016/S0003-2670(00)01115-6.

16 R. Henrion, G. Henrion, P. Heininger and G. Steppuhn, Statistical Analysis of Complex Round Robin Tests, *Acta Hydrochim. Hydrobiol.*, 1991, **19**, 603–614, DOI: 10.1002/aheh.19910190604.

17 International Organization for Standardization (ISO), *Accuracy (Trueness and Precision) of Measurement Methods and Results*, (ISO 5725-2:2025), 2025.

18 K. Sakurai and A. Kurokawa, Round-robin layer-thickness determination: Toward reliable reference-free X-ray spectrometry, *X-Ray Spectrom.*, 2019, **48**, 3–7, DOI: 10.1002/xrs.2978.

19 B. Beckhoff, Reference-free X-ray spectrometry based on metrology using synchrotron radiation, *J. Anal. At. Spectrom.*, 2008, **23**, 845–853, DOI: 10.1039/B718355K.
20 K. Wasa, I. Kanno and H. Kotera, *Handbook of Sputter Deposition Technology*, William Andrew, 2012.
21 P. Gawlitza, S. Braun, S. Lipfert and A. Leson, in *Ion-beam Sputter Deposition of X-Ray Multilayer Optics on Large Areas*, SPIE Optics + Photonics, San Diego, California, USA, 2006.
22 A. Rack, T. Weitkamp, M. Riotte, D. Grigoriev, T. Rack, L. Helfen, T. Baumbach, R. Dietsch, T. Holz, M. Krämer, F. Siewert, M. Meduna, P. Cloetens and E. Ziegler, Comparative study of multilayers used in monochromators for synchrotron-based coherent hard X-ray imaging, *J. Synchrotron Radiat.*, 2010, **17**(4), 496–510, DOI: 10.1107/S0909049510011623.
23 M. Kaufmann, M. Mantler and F. Weber, Analysis of Multi-Layer Thin Films by XRF, *Adv. X Ray Anal.*, 1993, **37**, 205–212, DOI: 10.1154/S0376030800015706.
24 M. Krumrey, Design of a Four-Crystal Monochromator Beamline for Radiometry at BESSY II, *J. Synchrotron Radiat.*, 1998, **5**, 6–9, DOI: 10.1107/S0909049597011825.
25 F. Senf, U. Flechsig, F. Eggenstein, W. Gudat, R. Klein, H. Rabus and G. Ulm, A plane-grating monochromator beamline for the PTB undulators at BESSY II, *J. Synchrotron Radiat.*, 1998, **5**, 780–782, DOI: 10.1107/S0909049597020323.
26 H. Riesemeier, K. Ecker, W. Görner, B. R. Müller, M. Radtke and M. Krumrey, Layout and first XRF applications of the BAMline at BESSY II, *X-Ray Spectrom.*, 2004, **34**, 160–163, DOI: 10.1002/xrs.750.
27 U. Pietsch, V. Holy and T. Baumbach, *High-resolution X-Ray Scattering: from Thin Films to Lateral Nanostructures*, Springer Science & Business Media, 2004.
28 H. Markötter, M. Sintschuk, R. Britzke, S. Dayani and G. Bruno, Upgraded imaging capabilities at the BAMline (BESSY II), *J. Synchrotron Radiat.*, 2022, **29**, 1292–1298, DOI: 10.1107/S1600577522007342.
29 H. Markötter, B. R. Müller, A. Kupsch, S. Evsevleev, T. Arlt, A. Ulbricht, S. Dayani and G. Bruno, A Review of X-Ray Imaging at the BAMline (BESSY II), *Adv. Eng. Mater.*, 2023, **25**, 2201034, DOI: 10.1002/adem.202201034.
30 *ToF-SIMS: Materials Analysis by Mass Spectrometry*, ed. J. C. Vickerman and D. Briggs, SurfaceSpectra Limited, Manchester, 2nd edn, 2013.
31 DAkksD-K-15076-01-00, Helmut Fischer GmbH, 2022, https://www.dakks.de/de/akkreditierte-stelle.html?id=D-K-15076-01-00, accessed 18 July 2025.
32 M. Kolbe, B. Beckhoff, M. Krumey and G. Ulm, Comparison of reference-free X-ray fluorescence analysis and X-ray reflectometry for thickness determination in the nanometer range, *Appl. Surf. Sci.*, 2005, **252**, 49–52, DOI: 10.1016/j.apsusc.2005.01.112.
33 X. Lu, S. R. Daemi, A. Bertei, M. D. Kok, K. O'Regan, L. Rasha, J. Park, G. Hinds, E. Kendrick, D. J. Brett and P. R. Shearing, Microstructural Evolution of Battery Electrodes During Calendering, *Joule*, 2020, **4**(12), 2746–2768, DOI: 10.1016/j.joule.2020.10.010.
34 H. Buhr, L. Büermann, M. Gerlach, M. Krumrey and H. Rabus, Measurement of the mass energy-absorption coefficient of air for x-rays in the range from 3 to 60 keV, *Phys. Med. Biol.*, 2012, **57**, 8231–8247, DOI: 10.1088/0031-9155/57/24/8231.
35 J. Kossaifi, Y. Panagakis, A. Anandkumar and M. Pantic, TensorLy: Tensor Learning in Python, *J. Mach. Learn. Res.*, 2019, **20**, 1–6.
36 T. G. Kolda and B. W. Bader, Tensor Decompositions and Applications, *SIAM Rev.*, 2009, **51**, 455–500, DOI: 10.1137/07070111X.